

pubs.acs.org/acscatalysis Research Article

Enhancement of Electrochemical Nitrogen Reduction Activity and Suppression of Hydrogen Evolution Reaction for Transition Metal Oxide Catalysts: The Role of Proton Intercalation and Heteroatom Doping

Qingdong Li,[#] Oguz Kaan Kucukosman,[#] Qingquan Ma,[#] Junjie Ouyang, Pavel Kucheryavy, Hengfei Gu, Conor L. Long, Zhiyuan Zhang, Joshua Young, Jenny V. Lockard, Eric Garfunkel, Jianan Gao, Wen Zhang,^{*} and Huixin He^{*}



Cite This: ACS Catal. 2024, 14, 8899-8912



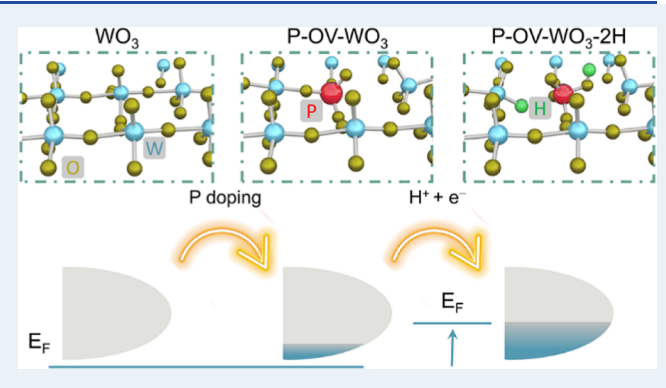
ACCESS

III Metrics & More

Article Recommendations

sı Supporting Information

ABSTRACT: During the electrochemical nitrogen reduction reaction (eNRR) and hydrogen evolution reaction (HER), interstitial proton intercalation readily occurs in some transition metal oxide (TMO) catalysts and changes their d-band electronic structure. This work fabricated phosphorus (P)-doped tungsten oxide (WO $_3$) with enriched oxygen vacancies (OVs) to study the impact of proton intercalation and heteroatom doping on eNRR and HER. Our results demonstrated that the electronic structure of the P-OV-WO $_3$ catalyst was altered by in situ proton intercalation as indicated by the greater negative onset potential of eNRR at -0.05 V compared to the proton intercalation potential of 0.3 V versus reversible hydrogen electrode (RHE). Compared to the non-P-doped WO $_3$, the introduction of P doping in WO $_3$ (e.g., 4.8



at. %) led to a reduction of more than 36% in proton intercalation. As a result, the HER activity of the P-OV-WO₃ was significantly suppressed, as demonstrated by a considerably negative shift of the onset HER potential from -0.06 to -0.15 V and a slower HER kinetics with the Tafel slope increased from 129.0 to 343.1 mV/dec. Density functional theory calculations revealed the synergy of the proton intercalation, substitutional P doping, and the associated OVs in the improvement of N₂ activation and hydrogenation in eNRR. The increased eNRR and the suppressed HER led to a high Faradaic efficiency (FE) of 64.1% and the NH₃ yield of 24.5 μ g·mg cat h⁻¹ at -0.15 V versus RHE in H₂SO₄ (pH = 2) as the electrolyte. The specific NH₃ yield is more than 20 times higher than that of C-WO₃ (1.1 μ g·mg cat h⁻¹ with a FE of 20%). The results exceed most of the reported eNRR performances for TMO-based catalysts. Thus, the synergistic proton intercalation and P doping could lead to newer designs and applications of TMO-based catalysts for improved eNRR while suppressing the competing HER.

KEYWORDS: substitutional doping, interstitial doping, proton intercalation, nitrogen reduction, transition metal oxides (TMOs), tungsten oxide nanosheets (WO₃)

1. INTRODUCTION

Ammonia (NH₃) is widely used as a feedstock for fertilizer production, alternative chemical hydrogen storage, and energy conservation materials, with an annual global production around 200 million tons per year. Currently, NH₃ is mainly synthesized via the Haber–Bosch process, an extremely energy- and capital-intensive process that operates at high temperatures of 400–500 °C and high pressures of 100–350 atm. This process consumes over 2% of the global annual energy output and emits a massive amount of greenhouse gases (~420 Mt CO₂ annually). Electrochemical nitrogen reduction reaction (eNRR) enables the production of NH₃ from nitrogen (N₂) and water (H₂O) under ambient conditions. Hence the storage of the storage of the global annual energy output and emits a massive amount of greenhouse gases (~420 Mt CO₂ annually). Electrochemical nitrogen reduction (eNRR) enables the production of NH₃ from nitrogen (N₂) and water (H₂O) under ambient conditions.

driven by renewable energies, eNRR could serve as a clean and sustainable strategy to substitute the traditional Haber–Bosch process for NH₃ production and potentially alleviate climate change. However, the application of eNRR to produce NH₃ in water-based solutions is still hindered by the low yield (mostly <10%), current density (mostly <1 mA cm⁻²)⁷ and Faradaic

Received: January 10, 2024 Revised: May 14, 2024 Accepted: May 14, 2024 Published: May 24, 2024





efficiency (FE) (mostly FE <15%),⁸ far below the U.S. Department of Energy's feasibility targets (e.g., current density >300 mA cm⁻² and FE >90%).⁹

One of the most critical challenges is to boost eNRR activity while suppressing or inhibiting the overwhelming competing side reactions such as the hydrogen evolution reaction (HER). Over the past few years, transition metal oxides (TMOs) have drawn increasing attention due to their earth abundance, synthesis simplicity, chemical stability, and tunable catalytic activity. TMOs are generally considered catalytically inert for HER, 10 and are thus ideal for the development of eNRR catalysts with high selectivity. To improve the eNRR activity of TMOs, introducing oxygen vacancies (OVs) and substitutional doping of heteroatoms on the surface and matrix of TMOs have commonly been employed. 11 It was reported that the transition metal centers can trap electrons due to the loss of O atoms (or generation of OVs) and thus could efficiently inject electrons into an antibonding orbital of adsorbed N2, which weakens the N≡N triple bond for subsequent hydrogenation. 12-14 OVs also provide coordinatively unsaturated sites and enable chemisorption of N₂. 12-14 Substitutional heteroatom doping is usually accompanied by the generation of higher density of OVs. 15 Dopant atoms and OVs could jointly increase the electron filling and vary the energy levels of the d-band centers of TMOs. 11 These changes affect the adsorption of intermediates, such as *N2H on the catalytic centers and catalytic reaction kinetics. Other strategies are also actively being pursued to tune the d-band center to improve the eNRR kinetics. As an example, Yan et al. recently fabricated WS₂-WO₃ heterostructures and efficiently upshifted the dband center of W in the interfacial electric field between WS₂-WO3 layers, which was shown to enhance the adsorption of intermediates (*NH2 and *NH) and accelerated eNRR kinetics.16

Besides OVs, heteroatom dopants, and the above-mentioned interfacial electric fields, the electronic structure of TMOs can also be modified by in situ proton intercalation, which has largely been overlooked in eNRR studies. 15-17 For example, WO3 readily undergoes bulk hydrogen intercalation in a cathodic electrochemical environment. ^{18–20} In fact, electrochemically induced interstitial proton intercalation/deintercalation $(xH^+ + xe^- + TMO \leftrightarrow H_xTMO)$ has been the working principle behind their applications in supercapacitors and electrochromic-based smart windows. 19,211 Associated with proton intercalation, the injected electrons would occupy the lowest empty states at the bottom of the conduction band of TMOs.²² Since the d orbital of the transition metal centers is the major contributor to the bottom of conduction band of TMOs, intercalation results in electron population of the d orbital of the transition metal centers of TMOs and upshift of Fermi level (E_F) . As a result, the d band center was relatively downshifted near or above its $E_{\rm F}$. ²² McKone and Mpourmpakis groups demonstrated that the in situ-achieved proton intercalation enabled HER on the intrinsically HER inert WO3, and the HER kinetics can be controlled by the level of proton intercalation. 18,23 In line with these studies, the Augustyn group developed approaches to modulate the HER activity of WO₃ by altering their proton intercalation behavior.²⁴ Since the level of electron population in the dband and the position of the d-band centers are also the descriptors for the eNRR catalytic activity of an electrocatalyst, 16,25-28 the large electronic changes resulting from bulk

proton intercalation would also affect eNRR, which has yet to be studied both experimentally and theoretically. $^{15-17}$

This work fabricated P-doped WO₃ nanosheets. The P doping process introduced P atoms and induced a substantial number of OVs within the WO3 matrix. The resulting product is thus termed P-OV-WO3, which was used as a representative proton-intercalated and substitutionally doped TMO. By contrast, WO₃ was employed as a representative protonintercalated TMO without substitutional doping in this study to investigate the roles of proton intercalation and substitutional doping (P doping) in tuning the electronic structure of WO₃, and their impacts on their HER and eNRR activities. The performance of these catalysts was evaluated with a N₂ flow electrolysis cell with gas diffusion electrodes to alleviate the poor solubility of N₂ in aqueous based electrolytes.²⁹ Extensive control experiments, including ¹⁵N isotopic labeling experiment using 15N2 as feed gas have been performed and confirmed that the measured NH3 was generated from electrochemical reduction of the feeding N2. Cyclic voltammetry (CV) was used to study the proton intercalation/ deintercalation and the associated HER of these catalysts. A rotating ring-disk electrode (RRDE) was further employed to elucidate the relationship between proton intercalation and HER activity by selectively decoupling the HER current contribution from the total measured currents on the disk electrode, which includes contributions from both HER and proton intercalation. Density functional theory (DFT) calculations were performed to analyze the synergistic role of interstitial proton intercalation, substitutional P doping, and the existence of OVs in tuning the electronic structures of TMOs for the enhancement of eNRR.

2. EXPERIMENTAL SECTION

2.1. Fabrication of P-OV-WO₃ and C-WO₃ Catalysts. To fabricate P-OV-WO₃, a gas—solid phase reaction approach was developed to avoid contamination of the surface of final products.^{30–33} Briefly, red phosphorus and tungstic acid (H₂WO₄ or WO₃·H₂O) nanosheets were selected as the doping source and precursor, respectively. The H₂WO₄ nanosheets were first fabricated via a hydrothermal method with a slightly modified protocol as described in Supporting Information S1.³⁴ A vertical furnace reactor was used for the P doping and the C-WO₃ catalysts, as depicted in Scheme S1, with additional details provided in Supporting Information S2.

2.2. Assessment of eNRR. The eNRR performance of the C-WO₃ and P-OV-WO₃ catalysts was evaluated using a CH Instruments 760E Potentiostat with a homemade designed N₂ flow electrolysis cell as shown in Figure S2a. This cell consists of a proton exchange membrane (Nafion 211, the Fuel Cell Store), a catalyst-coated GDE, a Pt plate, and an Ag/AgCl (saturated KCl) electrode as the working electrode (WE), counter electrode (CE), and reference electrode, respectively. The GDE was prepared by drop-casting the catalysts ink onto a piece of carbon paper (CP) $(0.7 \times 0.7 \text{ cm})$ as explained in Supporting Information S4. The GDE was used to alleviate the low solubility issue of N_2 in water (0.71 mg/mL),²⁹ by passing pressurized N₂ gas with a flow rate of 2.5 mL/min through a H_2SO_4 (0.1 M) solution to trap any possible NH₃ in the N₂ tank and then purged the back side of the GDE (the side without catalyst coating) for eNRR. The excess gas was purged back to the electrolyte to avoid the loss of the produced NH3 carried over by the N2 flow during the eNRR. The WE side and the CE side were separated by a Nafion 211 membrane.

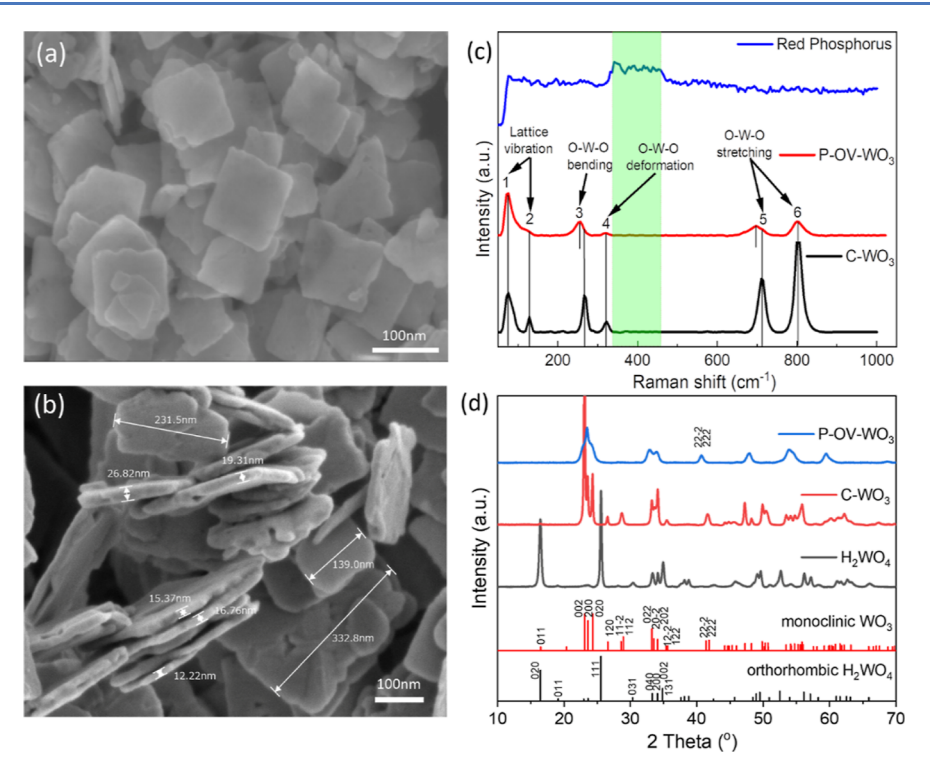


Figure 1. (a,b) Representative SEM images of P-OV-WO₃. (c) Raman spectrum of red phosphorus, P-OV-WO₃, and C-WO₃, respectively. (d) PXRD spectrum of P-OV-WO₃, C-WO₃, and H₂WO₄, and pdf card of monoclinic WO₃ and orthorhombic H₂WO₄.

The electrolysis was performed for 1 h with constant potential in a H_2SO_4 solution (5 mM, pH 2) as the electrolyte. The pH of the electrolyte solution was optimized at -0.15 V to pH = 2 electrolyte (Figure S3a). The electrolyte in the WE side of the cell was collected for ammonium (NH₄⁺) and hydrazine (N₂H₄) detection using the indophenol blue UV–vis spectroscopy method, NMR spectroscopy, and the Watt–Chrisp method as detailed in Supporting Information S6–S8. The NH₃ yield rate and the FE for the nitrogen–ammonia conversion were calculated as detailed in Supporting Information S5.

Control experiments were performed to examine the potential release of NH3 or NH4+ from CP, as well as any possible contamination from the electrolyte, the electrolysis cell, or the N2 gas feed. Three experimental conditions were evaluated, including (1) the use of the CP without loading the catalyst as the WE to run electrolysis at -0.15 V with N_2 ; (2) the use of the P-OV-WO₃ modified CP as the WE to run electrolysis with N₂ but keep the potential at open circuit potential; and (3) the use of P-OV-WO₃ modified CP as the WE to run electrolysis at -0.15 V but in Ar flow. Lastly, a 15 N isotopic labeling experiment was performed using ¹⁵N₂ as the feed gas. The resulting product was analyzed using ¹H NMR spectroscopy, leveraging the distinct characteristic features between 15NH₄+ and 14 NH₄+ in NMR spectroscopy to further confirm the N source of the NH₄⁺ product originated from the feed N₂ through eNRR. To quantify the NH₄⁺ derived from eNRR via the NMR method, a standard curve (Figure S4) was generated with maleic acid used as an internal standard.

2.3. Study of Proton Intercalation and Associated HER. HER as the major competing reaction during eNRR was reported to cause both low FE and low eNRR activity. Due to the faster kinetics of HER, the catalytic surface is quickly occupied by H₂ nanobubbles from HER, which could block N₂

to access the catalytic centers.³⁵ As reported by McKone and Mpourmpakis,23 HER on WO3 based catalysts is a consequence of bulk proton intercalation. To understand the different specific NH3 yield rates and FE of P-OV-WO3 and C-WO₃, the proton intercalation/deintercalation and HER characteristics of these two catalysts were studied via CV at scan rates of 10-100 mV s⁻¹ in an Ar-saturated electrolyte (5 mM H_2SO_4 , pH = 2). Linear sweep voltammetry (LSV) with a RRDE was also employed for the study to better identify the onset potentials of HER by decoupling the current contributions from proton intercalation and HER. The RRDE consisted of a 4 mm diameter glassy-carbon disk surrounded by a Pt ring, provided by ALS Co. Ltd. in Tokyo, Japan, and equipped with a RRDE-3A system from the same company. A total of 10 μ L of the catalyst ink was deposited only onto the disk electrode by using the same deposition process as in the CV measurements. During the LSV experiments, the voltammograms on the disk electrode were collected at 10 mV s⁻¹, while the potential on the ring electrode was maintained at 0.89 V versus reversible hydrogen electrode (RHE). The "true" onset HER potential, defined as the potential at which the ring current density reached 1 μ A.cm⁻², was marked on the ring current curves of C-WO₃ and P-OV-WO3, respectively. All other experimental procedures remained consistent with those employed in the CV measurements.

3. RESULTS AND DISCUSSION

3.1. Characterization of P-OV-WO₃ and C-WO₃ Catalysts. Figure 1a,b shows the representative SEM images of the P-OV-WO₃ nanocatalyst, which are square nanosheets with length of 100-350 nm and thickness of approximately 10-30 nm. These structures closely resemble those of the precursor H_2WO_4 , as shown in Figure S1a. The shape of the C-

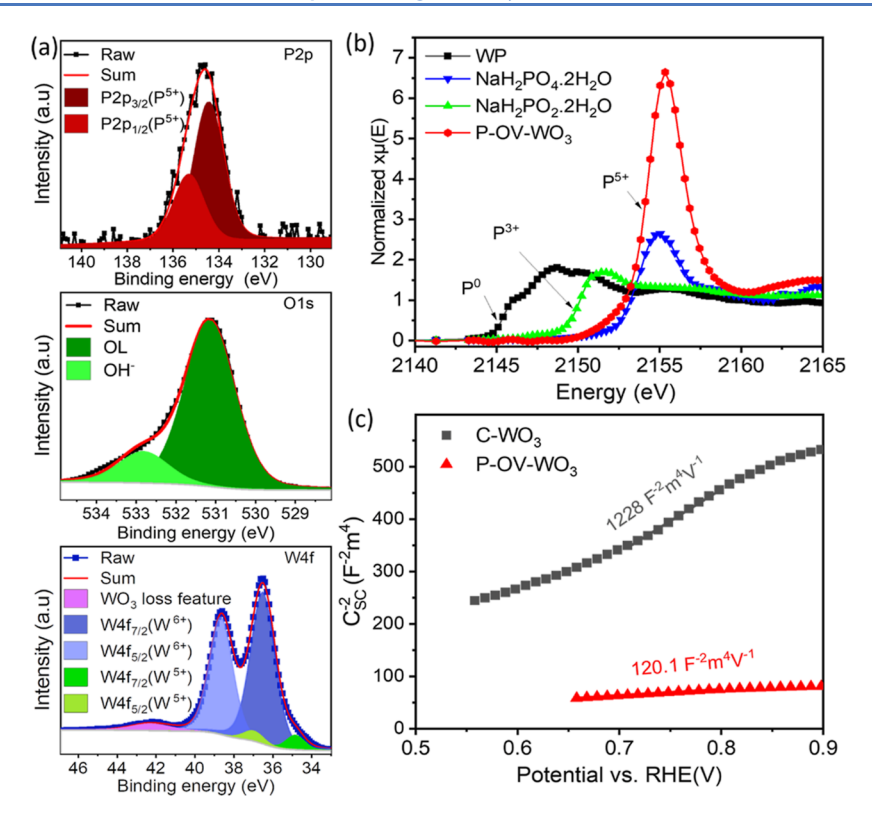


Figure 2. (a) XPS spectra of P 2p, O 1s, and W 4f of P-OV-WO₃. (b) XANES of P-OV-WO₃ and reference samples. (c) Mott–Schottky plots of the P-OV-WO₃ and C-WO₃.

WO₃ also largely remains, except that the corners of the square nanosheets became slightly rounded (Figure S1b). Raman spectroscopy was first applied to examine if there is any elemental phosphorus or P(0) condensed on the P-OV-WO₃, which has been very common in literature. 30,36,37 As shown in Figure 1c, the characteristic broad peak (350-460 cm⁻¹) in the Raman spectrum of red phosphorus was absent in the spectrum of the P-OV-WO₃ catalyst, suggesting that the designed protocol and cleaning procedures effectively prevented contamination of the final product by the residue of P(0). This conclusion was further confirmed by the X-ray photoelectron spectroscopy (XPS) results in the following section. The Raman spectra of C-WO₃ and P-OV-WO₃ was compared to reveal their structural difference. The intensity of the peaks in these spectra was normalized by the intensity of peak 1 for convenient comparison. The peaks at 76 and 128 cm⁻¹ were assigned to the lattice vibration of WO₃.³⁸ Peak 3 and peak 4 at 265 and 322 cm⁻¹ were assigned to the O-W-O bending and deformation modes, respectively.³⁸ Peak 5 and peak 6 at 712 and 802 cm⁻¹ were assigned to the O-W-O stretching modes corresponding to the long W-O bond and short W-O bond in the quasi-octahedra of WO₆ in WO₃ materials, respectively. Peak 3, the O-W-O bending mode, and peak 5, the O-W-O stretching mode for the long W-O bond of P-OV-WO3 sample, are red-shifted to 254 and 696 cm⁻¹, respectively, indicating that the bond length of the longer W-O was increased in the P-OV-WO₃ sample.

The crystal structures of C-WO $_3$ and P-OV-WO $_3$ were further characterized via powder X-ray diffraction (PXRD). The PXRD pattern of C-WO $_3$ in Figure 1d displays a well-defined monoclinic crystal structure, which is different from that of the precursor H_2WO_4 (e.g., a purely orthorhombic phase). Clearly, a phase transition has occurred to the

precursor H₂WO₄ during the heating process.³⁹ P-OV-WO₃ also exhibited a monoclinic crystal structural pattern. However, the peaks associated with P-OV-WO3 are notably broadened with significantly reduced intensities. This suggests that P doping within WO3 may have reduced its crystallinity. We also noticed that the peak at 41.7° [corresponding to $(2\ 2\ -2)$ and (2 2 2) planes in C-WO₃ shifted to 40.7° in P-OV-WO₃, indicating that the interplane distance for $(2\ 2\ -2)$ and $(2\ 2\ 2)$ planes has increased and some of the W-O bonds in P-OV-WO₃ elongated upon P doping. This is consistent with the Raman analysis showing that the bond length of the longer W-O was further increased in the P-OV-WO₃ sample (Figure 1c). This increased bond length may be attributed to the relatively smaller size of P⁵⁺ (52 pm) than those of W⁵⁺ (76 pm) and W⁶⁺ (74 pm). As the P atoms replace some of the W atoms in the WO₃ lattice, P⁵⁺ would attract the connected O closer due to its stronger affinity to O and thus result in slightly longer W-O bonds surrounding the P-substituted parts.

XPS analysis was carried out to investigate the surface compositions (<10 nm in depth) and oxidation states of P and W in both C-WO₃ and P-OV-WO₃. The XPS spectrum of P 2p contains one doublet pair of 2 $p_{3/2}$ and 2 $p_{1/2}$ peaks, which corresponds to P(V) or phosphorus in the +5 oxidation state (Figure 2a). The absence of peak at 130 eV indicates no detectable elemental P [P(0)] in the P-doped samples, suggesting that no condensation of P(0) on the doped WO₃ surface occurred, consistent with the Raman studies described above. The oxidation state of P in the bulk crystal is further confirmed by X-ray absorption near edge structure (XANES) in Figure 2b. The P-OV-WO₃ samples show the same P edge as the reference sample of NaH₂PO₄·2H₂O₅, suggesting that even in the bulk crystal, P is in the 5+ oxidation state. As a nonmetal element, P is commonly expected for

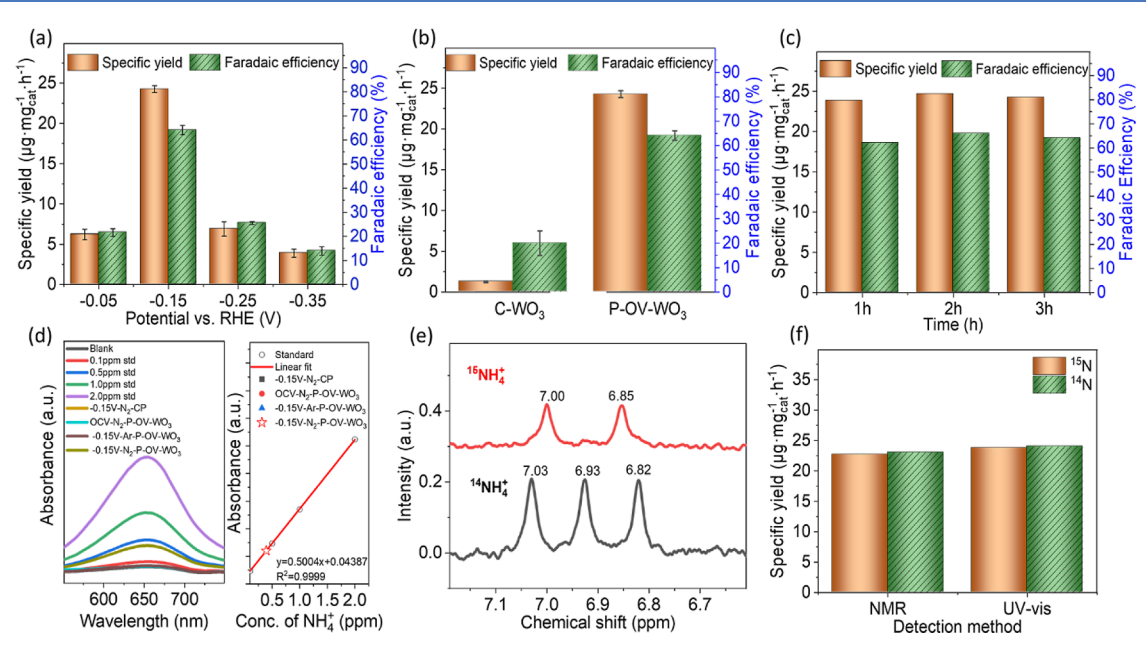


Figure 3. (a) NH₃ specific yield rate and faradic efficiency of P-OV-WO₃ at different cathodic potentials. (b) Comparison of the eNRR performance of C-WO₃ and P-OV-WO₃ under identical conditions (at -0.15 V). (c) Specific yield rate and faradic efficiency of P-OV-WO₃ in three consecutive cycles. The electrolyte for these experiments was H₂SO₄ solution (pH = 2), which was first purged with Ar to remove O₂ and then saturated with N₂. (d) UV-vis spectra of the electrolytes collected from the various control experiments following the indophenol blue spectrophotometric method. (e) ¹H NMR spectra of the electrolytes after eNRR electrolysis on P-OV-WO₃ using ¹⁵N₂ (top) and ¹⁴N₂ (bottom) as the feeding gas, respectively. (f) Comparison of the measured specific yield rate and faradic efficiency via the NMR and indophenol blue spectrophotometric method.

anionic doping via the substitution of O in the WO_3 lattice, resulting in the formation of W–P bonds. The electronegativity of W (2.36) and P (2.19) are close; thus, in the W–P bond, the oxidation state of P should be close to 0. However, the absence of P(0) and presence of P(V) indicate that no W–P bond was formed, meaning the P-substituted W instead of O in the P-OV-WO $_3$ lattice. Indeed, Table S1 shows that the atomic percentage of W decreases as the P doping level increases. Therefore, cationic doping was achieved instead of the commonly expected anionic doping in WO $_3$, which was also observed in P doping of TiO $_2$.

Since P(V) is one valence lower than the W(VI), OVs are introduced concurrently to maintain the charge balance during P doping, which was also observed for cationic metallic doping. 41 The XPS spectrum of the O 1s peak in Figure 2a was deconvoluted into two major peaks. The main peak at 531.1 eV is assigned to the lattice oxygen (OL). The peak at 532.6 eV is ascribed to hydroxyl groups (OH-) that were likely due to the water adsorption at the surface and defect parts, especially at OVs. 42 Table S1 shows that the atomic ratio of OH⁻/O (the total oxygen) for P-OV-WO₃ was calculated from their integrated XPS peak area to be 0.18, much higher than the 0.05 found for the control sample ($C-WO_3$). The high ratio of OH⁻/O indicated a high concentration of OVs, and defects were introduced during P-doping. Also, the surface composition of P-OV-WO3 without the adsorbed oxygen is calculated to be (W/P) O_{1.93}, which again demonstrated a much higher oxygen deficiency in P-OV-WO3 as compared to the control sample (WO_{2.19}) (Table S1).⁴² The existence of higher OVs and defects in the P-OV-WO₃ is consistent with its apparent dark blue color.43 The spectrum of W 4f in Figure 2a was deconvoluted into two doublet pairs, which correspond to W(VI) and W(V), respectively. A higher W(V)/W(VI) ratio is found in P-OV-WO₃ than that in C-WO₃, suggesting that P

doping also resulted in the generation of low valence W(V) besides OVs, which jointly yielded a higher electron density in P-OV-WO₃ than that in C-WO₃. 44

The electron density of the two catalysts was measured via Mott-Schottky plots under dark conditions, where the charge carriers in a semiconductor are exclusively contributed from dopants and vacancies. Thus, the donor density (N_D) is a direct measure of the electron density in the conduction band of n-type doped semiconductors.⁴⁵ Figure 2c shows that both the Mott-Schottky plots of the P-OV-WO₃ and C-WO₃ have a positive slope, suggesting that they are n-type semiconductors. The slope of P-OV-WO₃ is much lower than that of C-WO₃, indicative of a higher electron density of P-OV-WO3. The calculated $N_{\rm D}$ of P-OV-WO₃ is 5.87 \times 10²⁶ m⁻³, about 10 times higher than that of C-WO₃ (5.74 \times 10²⁵ m⁻³). The higher electron density in the conduction band may thus provide more available electrons entering the antibonding- π^* orbital of N_2 through π back-donation and more effectively activate the N_2 by weakening the $N \equiv N$ triple bond.

3.2. eNRR Performances of C-WO₃ and P-OV-WO₃ Catalysts. The NH₃ yield rate and FE of P-OV-WO₃ catalyst at different cathodic potentials are shown in Figure 3a. As the cathodic potential increased from -0.05 to -0.35 V, both the specific yield rate and FE exhibited an initial increase followed by a subsequent decrease, peaking at -0.15 V. Compared with C-WO₃, the P-OV-WO₃ catalyst exhibited improved eNRR activity as the FE has reached 64.1% (green bar) with the NH₃ yield of 24.5 μ g mg $_{cat}^{-1}$ h⁻¹ (orange bar) at the cathodic potential of -0.15 V versus RHE (Figure 3b). The specific NH₃ yield rate for P-OV-WO₃ is over 20 times of C-WO₃ (1.1 μ g mg $_{cat}^{-1}$ h⁻¹ with a FE of 20%) and around 6 times of those reported WO₃ with only OVs (4.2 and 4.9 μ g mg $_{cat}^{-1}$ h⁻¹ with FE of 12.8 and 23%, respectively). 46,47 The eNRR performance of C-WO₃ at other potentials was also studied. As shown in

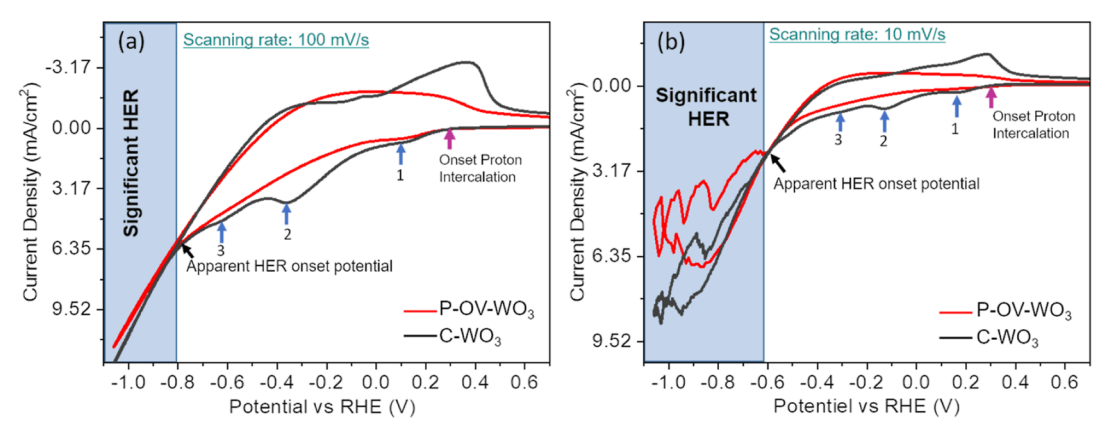


Figure 4. CV of C-WO₃ and P-OV-WO₃ with scan rates of 100 (a) and 10 mV/s (b). All of the curves and arrows in this figure are color coded: the black curves for C-WO₃ and red curves for P-OV-WO₃. The blue arrows point to the potentials for peaks #1, 2, and 3, respectively. The black arrows point to the apparent HER onset potential, and the pink arrows point to the onset potentials of the first proton intercalation peaks in each curve

Figure S3b, C-WO₃ at all other potentials studied exhibited significantly lower specific yield rates and FE than those of P-OV-WO₃ except at -0.05 V. At this potential, the C-WO₃ catalyst showed a higher FE (38% vs 21.6%), but the yield was still much lower (1.1 $\mu g \cdot mg_{cat}^{-1} h^{-1} vs 6.21 \, \mu g \cdot mg_{cat}^{-1} h^{-1})$. Atomic thin two-dimensional (2D) nanomaterials are well-known to have the highest accessible catalyst sites to reactants due to their atomic thickness. It is worthwhile mentioning that this performance reported here is even higher than that achieved by the atomic thin two-dimensional (2D) WO₃ nanosheets with OVs (17.28 μg mg $_{cat}^{-1}$ h $^{-1}$ with a FE of 7.0%), representing one of with the highest NRR performance of among the reported WO₃-based NRR catalysts as summarized in Table S2. $^{46-48}$

The catalyst stability was studied by monitoring the FE and NH_3 yield rates at a fixed cathodic potential of -0.15 V. Figure 3c indicates that both the FE and NH3 yield rate remained almost unchanged with 3 times of electrolysis (1 h/each time). Beyond that, both the measured FE and NH3 yield drastically decreased likely due to flooding of the gas diffusion layer (GDL) of the CP on which the catalysts have deposited (Experimental 2.3). As shown in Figure S5, after three times of electrolysis (1 h/time), most of the time we observe a current increase (Figure S5b), and the current increase gets faster with more time of electrolysis (Figure S5c,d). GDL flooding at negative potentials, especially in highly acidic environments is a commonly encountered issue. 49 Nevertheless, extensive control experiments were performed, as described in Section 2.2. All the control experiments yielded negligible NH₄⁺ as shown in Figure 3d and confirmed that the detected NH₄+ originated from eNRR. Lastly, a ¹⁵N isotopic labeling experiment was performed using ¹⁵N₂ as feed gas to further confirm the N source of the NH₄⁺ product; Figure 3e shows the ¹H NMR spectra for the electrolytes after eNRR electrolysis on P-OV-WO₃ using ¹⁵N₂ (top), where we observed two characteristics peaks corresponding to ¹⁵NH₄⁺ (δ = 6.85 and 7.00 ppm). On the other hand, the characteristic peaks corresponding to $^{14}\mathrm{NH_4}^+$ (at $\delta = 6.82$, 6.93, and 7.03 ppm) were observed when ¹⁴N₂ was used as the feed gas. The production rates of ¹⁵NH₃ and ¹⁴NH₃ measured via the NMR method were consistent with the UV-vis results obtained via the indophenol blue spectrophotometric method (Figure 3f). All of these results together confirmed that the measured NH₄⁺

in the electrolyte was produced from electrochemical reduction of the N_2 feed stream by the P-OV-WO₃ catalysts.

3.3. Analysis of Impacts of Proton Intercalation and HER on eNRR via Cyclic Voltammetry Studies. Figure 4a shows three reduction peaks as marked as the peak (1-3) on the black curve for C-WO₃ that correspond to different intercalation stages. 18,23 Furthermore, a pronounced current increase occurred at approximately -0.8 V versus RHE under the scanning rate of 100 mV/s, which could be the onset potential of "significant HER" as suggested by Mpourmpakis et al. 18,23 The "significant HER" potential region was shaded in blue. The onset potential for the "significant HER" was denoted as "apparent" HER onset potential to differentiate from the "true" HER onset potential, which is introduced in the RRDE section below. At a lower potential scanning rate of 10 mV/s, both the peak potentials for proton intercalation and the "apparent" HER onset potential shifted toward more positive values as shown in Figure 4b, very likely due to the decreased limitation in proton mass transportation in the electrolyte and smaller uncompensated resistance. ⁵⁰ Moreover, the CV curves exhibited an erratic pattern in the "significant HER" potential region from -0.6 to -1.05 V due to the mechanical disturbance caused by the detachment of hydrogen bubbles during the CV measurements that could induce abrupt changes of the current.

For P-OV-WO₃, a proton intercalation peak was also observed at ~0.11 V, which is similar to the first intercalation peak marked as peak 1 on the black curve for C-WO3. The onset potential for this peak of 0.3 V is also similar for these two catalysts, as marked by the pink arrow in Figure 4a. The intercalation peaks at -0.35 and -0.62 V did not show up as they did on the black curve as marked as the peaks 2 and 3, respectively. The intercalation currents for P-OV-WO3 under both scanning rates in Figure 4a,b were substantially lower than those of C-WO₃. This demonstrates that P doping interfered with or reduced the proton intercalation within WO3. To quantitatively assess the reduction of proton intercalation, we calculated the amount of charge transfer associated with the first proton intercalation peak (peak 1) during the cathodic scan of the CV curves for both the P-OV-WO₃ and C-WO₃ catalysts. Figure S6 shows that the charge transfer associated with the first proton intercalation peak in P-OV-WO₃ is roughly 64% of the charges for C-WO₃ as depicted by the green shaded region, suggesting proton intercalation in

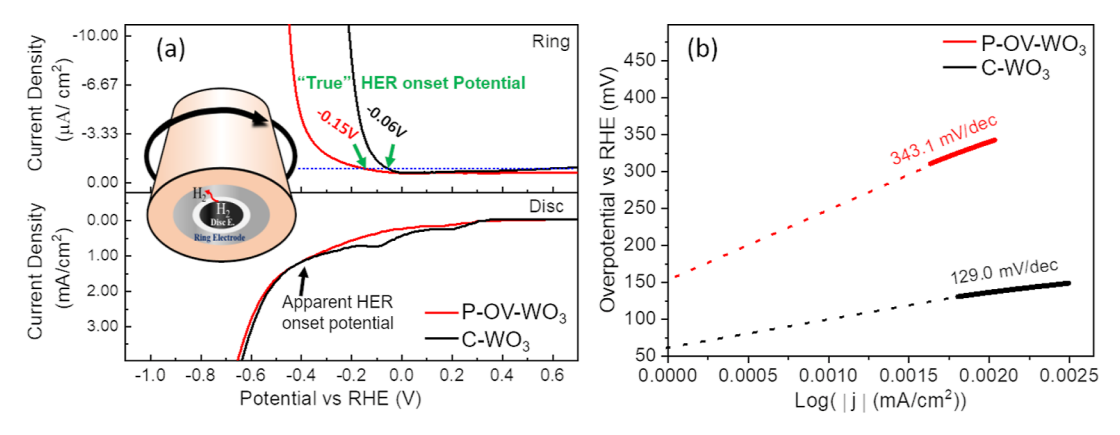


Figure 5. (a) RRDE voltammograms of C-WO₃ and P-OV-WO₃ at a rotation speed of 1600 rpm. The negative-going polarization curves on the disk electrodes were collected at 10 mV/s (bottom), while the ring potential was held at +0.89 V (top). Inset (a) shows a schematic drawing of a RRDE. (b) Corresponding Tafel slopes of C-WO₃ and P-OV-WO₃ derived from the ring electrode. All the curves and arrows in this figure are color coded: the black curves for C-WO₃ and red curves for P-OV-WO₃. The black arrow points to the apparent HER onset potential, and the green arrows in (a) upper point to the "true" HER onset potentials of the two catalysts.

P-OV-WO $_3$ was reduced by about 36%. We selected the first proton intercalation peak for this estimation because the second and third proton intercalation peaks are likely associated with certain levels of HER as demonstrated in the RRDE studies described below. The total decrease of proton intercalation in the full intercalation potential range of 0.3 to -0.8 V is likely higher than 36%.

Figure 4a,b shows that the onset potentials of proton intercalation for both catalysts (+0.30 V) are more positive than that of eNRR (-0.05 V) shown in Figure 3a, which clearly demonstrated that proton intercalation already started at the potentials of eNRR. Therefore, the role of proton intercalation in turning the electronic structure of the WO₃ based catalysts for eNRR cannot be ignored. Figure 4a,b also illustrates that the "apparent" HER onset potentials were notably higher than the onset potential of proton intercalation (+0.30 V). This observation agrees with the findings reported by McKone and Mpourmpakis, 18,23 which indicated that proton intercalation enabled the HER activities of WO₃. On the other hand, the "apparent" onset potentials for the "significant HER" (>-0.6 V) were notably more negative than the eNRR potentials ($-0.05 \sim -0.25 \text{ V}$) as shown in Figure 3a, which suggested that HER have been suppressed at the eNRR potentials. Consequently, its impacts on the performance of eNRR were largely reduced, offering a reasonable explanation for the observed high FE (64.1%) for the P-OV-WO₃ catalyst. However, this does not explain well the low FE (20%) observed for the C-WO₃ catalyst. Thus, we conducted a Watt-Chrisp test to check if hydrazine, a potential byproduct, was generated during eNRR for both catalysts. The absence of detectable hydrazine in the eNRR products indicates that the observed low FE was not due to this side reaction of hydrazine production. Hence, it is plausible that HER may have taken place at the potentials of eNRR, implying that HER might have initiated at potentials notably less negative than the "apparent" HER onset potentials observed. An improved method is needed to accurately identify the "true" HER onset potentials and understanding the competition of HER during the eNRR of these catalysts.

3.4. Reassessment of the HER Activities of C-WO₃ and P-OV-WO₃ Using Rotating Ring Disk Electrode Analysis. LSV were collected from the disk electrode of the RRDE that was coated with C-WO₃ and P-OV-WO₃, respectively. The

bottom part of Figure 5a indicates a similar behavior as observed in the CV curves collected at the same scan rate of 10 mV/s (Figure 4b), which reveals the occurrences of proton intercalation and "significant HER" at different applied potentials. One exception is that the peak potentials labeled in Figure 5a are positively shifted due to the electrode rotation, which improved the proton mass transport in the electrolyte. Moreover, the erratic current pattern in Figure 4b in the "significant HER" potential region was absent in Figure 5a as the electrode rotation effectively removed the generated H_2 before they formed H_2 bubbles on the disk electrode and thus reduced the bubble effect on the current measurements.

The upper part of Figure 5a shows the ring current as a function of the cathodic potentials on the disk electrode. The ring currents resulted from oxidation of H₂ (HOR) generated on the catalyst coated disk electrode, which then diffused onto the ring electrode. Therefore, the contribution of HER current reflected by the HOR current on the ring electrode and was decoupled from the total current that included both HER and proton intercalation currents in the LSV and disk current measurements. Given the potential on the Pt ring electrode was +0.89 V versus RHE, sufficiently positive to promptly oxidize the H2 diffusing onto the ring electrode from the disk electrode, we assume that the trend of the HOR kinetics measured on the ring electrodes can represent the trend of the HER kinetics on the disk electrodes, on which the C-WO₃ and P-OV-WO₃ catalysts were deposited. For the disk electrode coated with C-WO₃, the ring current became detectable when the cathodic potential on the disk reached -0.06 V. This potential of -0.06 V is denoted as the "true" HER onset potential of the C-WO₃ catalyst to differentiate the "apparent" HER onset potentials identified from Figure 4a,b and the bottom part of Figure 5a. For the P-OV-WO₃ catalyst, this "true" onset potential of the HER negatively shifted to -0.15V. Obviously, the "true" HER onset potentials for both catalysts are significantly more positive than their "apparent" HER onset potentials. More importantly, these results clearly demonstrated that the "true" HER onset potential for the C- WO_3 catalyst (-0.06 V) is close to its onset potential for the eNRR (-0.05 V). Considering the faster kinetics of HER than eNRR, severe HER competition is expected, which well explained the lower FE (20%) for the C-WO₃ catalyst. In high contrast, the "true" HER onset potential for the P-OV-WO₃

ACS Catalysis pubs.acs.org/acscatalysis Research Article

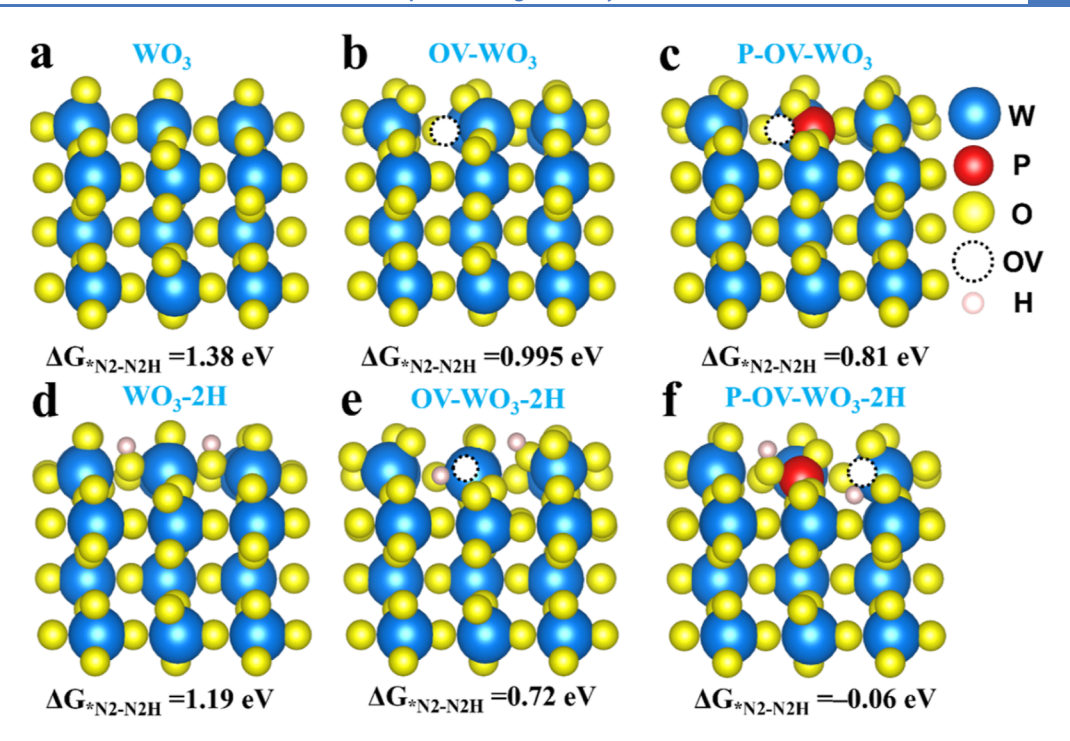


Figure 6. Optimized crystal structure: (a) WO₃, (b) OV-WO₃, (c) P-OV-WO₃, (d) WO₃-2H, (e) OV-WO₃-2H, and (f) P-OV-WO₃-2H.

catalyst (-0.15 V) is much more negative than the onset potential of eNRR (-0.05 V). Interestingly, it happens coincident with its peak eNRR performance as shown in Figure 3a. Furthermore, as the cathodic potentials on the disk electrode became more negative than the "true" onset HER potentials, the ring current for C-WO₃ initially increased with a Tafel slope of 129.0 mV/dec (Figure 5b) and then quickly entered into "the potential independent HER regime" at ~ -0.15 V as described by Mpourmpakis et al. For P-OV-WO₃, the initial ring current increased with a much higher Tafel slope of 343.1 mV/dec. It is important to clarify that in this context, the word "initial" here refers to the potential range studied for the Tafel slopes, which is significantly lower than the range where significant H2 bubbles are generated on the disk electrode, as shown in Figure 5. As a result, the influence of nonkinetic effects on deriving the Tafel slopes was minimal in this study.⁵¹ Since the trend of the initial HOR kinetics measured on the ring electrodes represents the trend of the initial HER kinetics on the disk electrodes, the higher Tafel slope indicated the HER kinetics of the P-OV-WO₃ catalyst was slower than that of the C-WO3. The large negative shift of the "true" onset potentials of HER in combination with the slower HER kinetics (Tafel slope = 343.1 vs 129.0 mV/dec) confirmed that P doping significantly suppressed the HER activity of WO₃, likely due to the considerably suppressed proton intercalation as discussed in Figures 4a,b and S5. The suppressed HER activity led to improved eNRR performance, as indicated by the increased specific yield rate and FE in Figure 3a,b.

3.5. Electronic Structure Analysis of Various Catalysts and Impacts on eNRR. DFT simulations were performed to further investigate the roles of O vacancies (OV), P substitutional dopping, and proton interstitial doping in tuning the electronic structures of WO₃ and the performance of eNRR. First, the (001)-terminated surfaces of WO₃, WO₃ with an O vacancy (OV-WO₃), and P-doped WO₃ with an O vacancy (P-OV-WO₃) were constructed as shown in Figure

6a-c, respectively. Next, two protons and two electrons were added to these surfaces to form WO₃-2H, OV-WO₃-2H, and P-OV-WO₃-2H in Figure 6d-f to represent their optimized structures upon proton intercalation.

For W-based oxides, 16 the first hydrogenation step of *N₂ to form and stabilize *N2H intermediates on the catalyst surface is the rate-determining step (RDS) for eNRR. 17,25,26,52 To evaluate the impacts of the surface atomic arrangements on eNRR, we first calculated the Gibbs free energy for *N2H formation $(G_{*N,H})$ with eq S4 (details in Supporting Information S11 and Table S3) on various constructed surfaces and summarized the results in Table S4. 17,25,26,52 As expected, the pristine WO₃ shows a large positive $G_{*N,H}$ (1.49) eV) as shown in Figure 6a, which indicates a high reaction energy barrier for the conversion of *N₂ to *N₂H ($\Delta G_{*N,-*N,H}$ = 1.38 eV) and thus the initial hydrogenation reaction may be restricted. Introducing an O vacancy to WO3 reduces the $\Delta G_{*N_2-*N_2H}$ value to 0.99 eV (Figure 6b). Notably, after incorporating a P dopant into OV-WO3 to form P-OV-WO3, the $\Delta G_{*N,-*N,H}$ level was reduced again to 0.81 eV (Figure 6c), which is expected to better promote the *N₂H intermediate formation on catalyst and eNRR. Due to the large gap (10.82 eV) from the highest occupied molecular orbital to the lowest unoccupied molecular orbital of N2, electron transfer from P to N₂ is unlikely to happen. Our calculations also confirmed that the P site has a positive adsorption energy for both N_2 (0.51) eV) and N_2H (0.36 eV). To gain a better intuitive view of the capture and activation capability toward N2, the activation energy of every *N2 to *N2H step was also calculated. As can be seen from Table S4, the largest activation barrier happens on the WO₃ surface which requires 1.21 eV and introducing an O vacancy to WO₃ reduces $\Delta G_{*N,-*N,H}$ to 1.16 eV. These results confirm that the heteroatomic dopants and OVs could both promote the initial step hydrogenation as reported previously.15

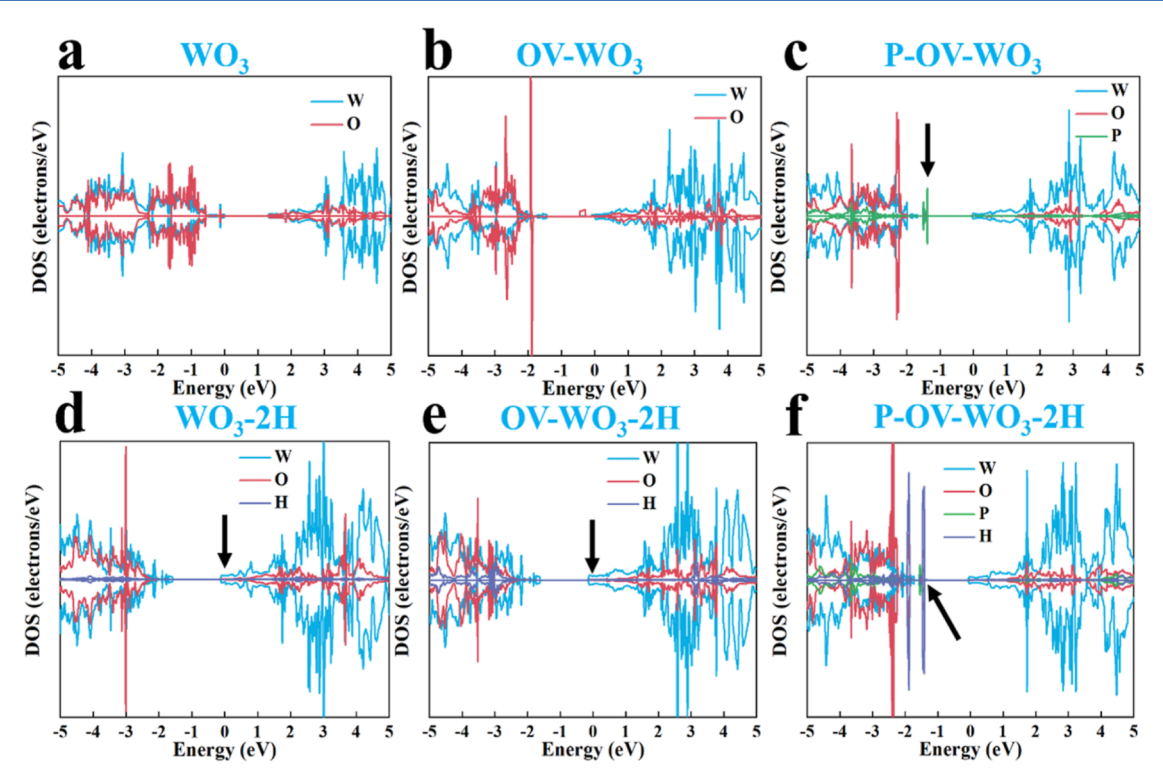


Figure 7. Density of states of (a) WO₃, (b) OV-WO₃, (c) P-OV-WO₃, (d) WO₃-2H, (e) OV-WO₃-2H, and (f) P-OV-WO₃-2H. The Fermi level is set as 0 eV, and black arrows point to the changing position of DOS.

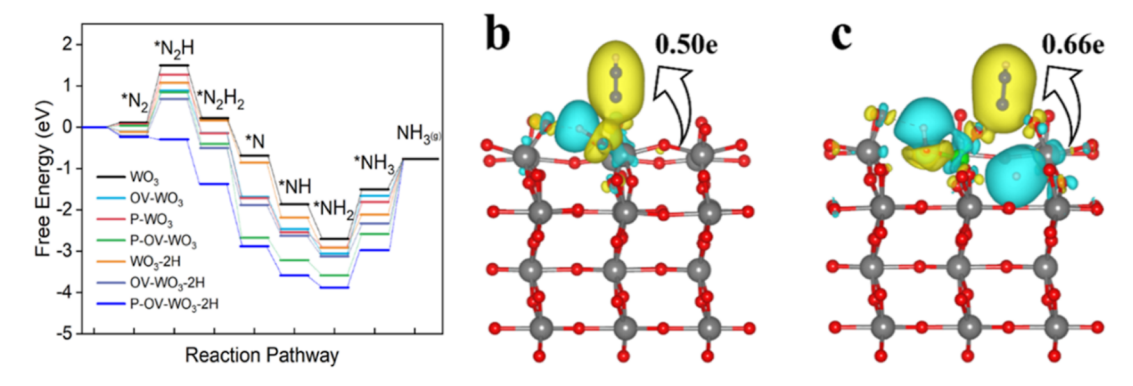


Figure 8. (a) Free energy diagrams of NRR distal pathway on WO₃, OV-WO₃, P-WO₃, P-OV-WO₃, WO₃-2H, OV-WO₃-2H, and P-OV-WO₃-2H. Charge density distributions of *N₂H adsorption on (b) WO₃-2H and (c) P-OV-WO₃-2H.

As the proton intercalation level increased when a more negative cathodic potential was applied, the increased electron population of the W d orbitals induces an increase of its Lewis acidity of the W sites. ^{18,23} As a result, the preferred binding sites of the intercalated proton switched from O to W leading to the formation of W-*H (adsorbed hydrogen atoms) in the WO₃ matrix and surfaces such as in Figure 6d-f. In the presence of N2, these W sites with high electron density may also act as catalytic centers to activate N2. The continuous proton intercalation provides hydrogen resources and the increased conductivity promotes hydrogenation of the activated N2 molecules (*N2) via the most commonly accepted proton coupled electron transfer mechanism.⁵³ The impact of proton intercalation on N2 adsorption and activation is also evident. The adsorption energies of N_2 (ΔG_{*N_2}) are also largely reduced for all these catalysts as shown in Table S4. Furthermore, each structure with intercalated H (Figure 6d–f) shows a more favorable N₂ hydrogenation step $(\Delta G_{*N_2-*N_2H})$

than the corresponding unhydrogenated structure (Figure 6ac). Moreover, the activation barriers for WO₃-2H, OV-WO₃-2H, and P-OV-WO₃-2H are 0.95, 0.91, and 0.76 eV, respectively. All of these activation barriers are even smaller than the reaction energy WO3 or PWO3, indicating that excellent kinetics can be expected after proton intercalation. These results are consistent with a previous conclusion that proton intercalation promotes hydrogenation of the activated N_2 molecules. However, the levels of $\Delta G_{*N,-*N,H}$ reduction are different. For example, upon proton intercalation of P-OV- $WO_3 \Delta G_{*N_2-*N_2H}$ decreased to -0.06 eV for P-OV-WO₃-2H (Figure 6f), which is significantly more negative than that achieved on C-WO₃ (WO₃-2H, 1.19 eV in Figure 6d), and on OV-WO₃ (OV-WO₃-2H 0.72 eV Figure 6e). These results indicate that the role of proton intercalation in tuning the electronic structures is highly dependent on the composition of the catalysts, which possibly explains the observed different eNRR yield rates (Figure 3b). In other words, the ex situ P-

substitutional doping, OVs, and the in situ proton intercalation synergistically boosted the eNRR activity of WO_3 catalysts. This improvement in the eNRR activity is also reflected in the full free-energy reaction diagrams calculated and shown in Figure 8.

To reveal the underlying mechanism of OVs and P-dopant on the electronic structures of WO₃, the projected density of states (PDOS) of the above contrasted surfaces were computed and are shown in Figure 7. For example, WO3 is a semiconductor with a finite band gap, where the d orbital of the W centers is the major contribution of the conduction band of WO₃ (Figure 7a). WO₃ is an n-type semiconductor. The Fermi level is the energy separating occupied states of the valence band from empty states of the conduction band at the absolute temperature T = 0 K. It has to shift toward the conduction band in an n-type semiconductor where the number of electrons n is higher than the number of holes (n > p). OV-WO₃ exhibits metallic character since the charge introduced by the OV defects enters the d orbitals of the W centers (Figure 7b). The introduction of the O vacancy results in the formation of empty states above the top of the valence bands. P-doping further shifts the maximum of the valence band of WO3 toward the Fermi level (0 eV) due to the presence of in-gap states as marked in Figure 7c. As the W atom is substituted by a P single atom and two more proton intercalation, the Fermi level is shifted up into the conduction bands, and a donor level is formed. Upon proton intercalation, noticeable electronic states even appeared at the Fermi level as pointed by the arrows in Figure 7d-f and may thus promote eNRR activity because the high DOS levels at the Fermi level can facilitate electron transport at the surface and the successive N2 reduction and the adsorption of intermediates according to the d band theory.²⁷ The affinity of TMO catalysts to bind N2 is affected by the coexisting empty and occupied d orbitals of transition metal atoms. The empty dorbitals of transition metal centers can accept lone-pair electrons of N2 to strengthen the TM-N bonds, while the occupied d orbitals can donate partial electrons into the antibonding orbitals of N_2 to weaken the $N \equiv N$.

To confirm the interactions between W-N orbitals, the PDOS of the W atom and N atom which directly connect *N₂H and different surfaces have been analyzed, as presented in Figure S9. The existence of OVs provides plenty of coordinatively unsaturated sites on WO_3 as compared to Figure 6. The unoccupied d orbitals of W atoms could accept some electrons from the adsorbed *N2H and form the W-N bonding states to strengthen the *N2H adsorption, as evidenced by the obvious hybridization between W and N orbitals around the Fermi level as shown in Figure S9b. Pdoping was also accompanied by the generation of higher density of OVs, which also increases the electron filling of the adsorbed *N₂H as shown in Figure S9c. Upon proton intercalation, Figure S9d-f shows the obvious enlarged PDOS of N orbitals, indicating that more electrons filled into the conduction band of the WO3 catalysts and were involved in the antibonding- π^* -orbital of *N₂H through π back-donation.⁵⁴ Overall, OVs and P-dopants in WO₃ have both proven effective toward weakening the N≡N triple bond and activating *N2H for subsequent eNRR more than that for C-WO₃. To further determine the underlying mechanism of N₂ activation on each surface, we carried out crystal orbital Hamilton population (COHP) calculations to reveal the bonding and antibonding contributions of the *N₂H

intermediate adsorbed on different surface. To provide a quantitative expression, we calculated the integrated COHP (ICOHP) between the N–N bond (Table S5). Note that the more positive ICOHP means the weaker *N_2 adsorption/activation, verifying the influence of the O vacancy, P dopant, and H intercalation on the bonding/antibonding populations. Similarly, the OVs and P-dopant demonstrated effectiveness in reducing the strength of the N \equiv N triple bond and enhancing the activation of *N_2 H for subsequent eNRR.

3.6. Evaluation of eNRR Reaction Pathways and Charge Transfer Mechanisms. The eNRR reaction pathways on the above constructed surfaces were proposed via a distal mechanism.⁵⁵ Among all elementary steps, the maximum ΔG appears in the first hydrogenation step, implying that the formation of *N₂H is the RDS for eNRR on the WO₃ surface. Although the last step for NH3 desorption is uphill for all surfaces, generated NH3 can be easily dissolved in water, favoring the release of NH3 from the catalyst surface and making *NH₂ → NH₃ still energetically efficient. Encouragingly, the dark blue line in Figure 8a shows that the RDS changed from *N₂H formation to NH₃ desorption for P-OV-WO₃-2H as indicated by the negative values of the Gibbs free energy (ΔG) change of the first protonation step $(\Delta G_{*N,-*N,H})$, as previously discussed in Figure 6. Phosphorus (P) doping, OVs, and proton intercalation on tungsten oxide (WO₃) all can effectively lower the reaction energy barrier and help to stabilize the *N₂H and significantly promote the initial hydrogenation reaction. Following the first protonation, all further steps are downhill in energy, indicating a facile transformation of *N2H into *NH3. The enhanced activity of the P-OV-WO₃-H system toward eNRR is therefore due to the fact that the ΔG of *N₂H formation is negative under these conditions (compared to the positive ΔG barrier observed in all other systems) owing to the increased activity of the W sites (see Section 3.5), leading to the favorable formation of NH₃. Furthermore, the presence of doped P, O vacancies, and intercalated H does not alter the barrier for desorption of NH₃, further supporting these conclusions.

Bader charge analysis was conducted to reveal electron transfer from the different catalyst surfaces to*N₂H in Figure 8b,c. Yellow and cyan regions indicate electron accumulation and depletion, respectively. Table S5 illustrates that the calculated charge transfer are all negative values and thus the electron transfer from each surface to the *N2H intermediate in each case. However, the charge transfer from P-OV-WO₃-2H to the N_2 H adsorbate (0.66e) (Figure 8c), is the highest in every case, such as that of WO_3 -2H (0.50e) (Figure 8b). The electron transfer is therefore enhanced with hydrogen intercalation, as indicated by the higher electron transfer after proton intercalation, suggesting an augmented electron donation from the catalyst surfaces to the *N2H intermediate in the presence of intercalated hydrogen. The smallest amount of charge transfer is observed for the bare WO3 surface (-0.48e), as expected (Table S5). Introducing a P dopant and an O vacancy in the WO3 surface results in slightly more charge transfer (-0.54e and -0.55e, respectively), to approximately the same degree; the presence of both together is higher than either alone (-0.61e). Intercalation of H slightly in WO3 and OV-WO3 surface increases the amount of charge transfer slightly (-0.50e and -0.56e, respectively), leading to the observations discussed in Figure 6. Finally, the combination of all together to create the P-OV-WO₃-2H

systems leads to the largest amount of charge transfer (-0.66e) and, when taken together with the DOS analysis (Figures 7 and S9), leads to the observed conclusions.

As the eNRR reaction is seriously limited by the competing HER, we also studied competing HER kinetics by reaction free energies for the Volmer step $(2H^+ + 2e^- \rightarrow H^* + H^+ + e^-)$ and Heyrovsky step $[H^* + H^+ + e^- \rightarrow H_2 (g)]$. The results in Table S7 show that P-OV-WO₃-2H has the highest energy barriers for H adsorption and desorption. These results are consistent with our experimental results, which show that HER activity of the P-OV-WO3 was significantly suppressed. Moreover, the side reaction of *N₂H₂ to *N₂H₄ has also been explored which confirms the reaction pathway of *N₂H₂ to *N + NH₃ is more favorable as shown in Table S7. These computational results suggest that the doping of P, creation of O vacancies, and intercalation of H in WO3 work synergistically to improve the observed eNRR performance and suppressing the HER. The combination of each of these factors together pushes the RDS of *N2 protonation to *N2H (Figure 7a) to be downhill in energy, and therefore much more energetically favorable, than in any other case, leading to the observed activity.

4. CONCLUSIONS

Using the P-doped WO3 as a model of intercalated TMObased catalysts, this work demonstrated that their electronic structure can be largely modified by in situ proton intercalation before eNRR. DFT calculations further revealed the role of interstitial hydrogen doping in tuning the electronic structure of the d band centers. The interstitial hydrogen doping, substitutional doping of P, and the existence of OVs together increased the electronic states of the d band around the Fermi level of the WO₃. Therefore, the reaction energy barrier in N₂ activation and hydrogenation was largely reduced, which, in turn, significantly improved the eNRR activities. On the other hand, P doping and the associated structural changes induce significant suppression of proton intercalation, indicated by the lower intercalation current compared to the nondoped WO₃. Consequently, the HER activity was efficiently suppressed, as demonstrated by the negative shift of the HER onset potential and the slow HER kinetics in the RRDE studies. Most importantly, at the optimal potential of eNRR at -0.15 V versus RHE, HER is barely started, which led to an unprecedentedly high FE of 64.1% with NH3 yield of 24.5 $\mu g \, m g_{cat}^{-1} \, h^{-1}$. It is worth mentioning that this work used WO₃ nanosheets of 200 nm square with a thickness of 10-30 nm, which is much larger than those used in some previous reports which demonstrated higher NH3 yields. 7,15 Significantly improved performance is expected if small nanoparticles or thinner nanosheets of one or a few layers were used to develop the catalysts. The new understanding of the mechanism for the observed performance enhancement provides more reliable guidelines for rational design of TMO and/or other intercalatable compounds (such as transition metal dichalcogenides) by taking consideration of the possible electronic modulation from both substitutional doping and in-operando proton and alkaline metal ion intercalation.

ASSOCIATED CONTENT

Supporting Information

The Supporting Information is available free of charge at https://pubs.acs.org/doi/10.1021/acscatal.4c00223.

Chemicals, experimental procedures for the fabrication and characterization of the catalysts, eNRR electrolysis, quantification of $\mathrm{NH_4}^+$ via the indophenol blue method and NMR methods, and quantification of $\mathrm{N_2H_2}$ via the Watt–Chrisp method and detailed DFT calculation (PDF)

AUTHOR INFORMATION

Corresponding Authors

Wen Zhang — Department of Civil and Environmental Engineering, New Jersey Institute of Technology, Newark, New Jersey 07102, United States; ⊚ orcid.org/0000-0001-8413-0598; Email: wen.zhang@njit.edu

Huixin He — Department of Chemistry, Rutgers, the State University of New Jersey, Newark, New Jersey 07102, United States; Email: huixinhe@newark.rutgers.edu

Authors

Qingdong Li — Department of Chemistry, Rutgers, the State University of New Jersey, Newark, New Jersey 07102, United States; occid.org/0000-0003-4089-7425

Oguz Kaan Kucukosman — Department of Chemistry, Rutgers, the State University of New Jersey, Newark, New Jersey 07102, United States; orcid.org/0000-0001-7795-5444

Qingquan Ma — Department of Civil and Environmental Engineering, New Jersey Institute of Technology, Newark, New Jersey 07102, United States; orcid.org/0000-0001-6879-6410

Junjie Ouyang — Department of Chemistry, Rutgers, the State University of New Jersey, Newark, New Jersey 07102, United States; oorcid.org/0000-0001-9417-6733

Pavel Kucheryavy – Department of Chemistry, Rutgers, the State University of New Jersey, Newark, New Jersey 07102, United States

Hengfei Gu – Department of Chemistry and Chemical Biology, Rutgers University, New Brunswick, New Jersey 08901, United States

Conor L. Long – Department of Chemistry, Rutgers, the State University of New Jersey, Newark, New Jersey 07102, United States

Zhiyuan Zhang — Department of Chemistry, Rutgers, the State University of New Jersey, Newark, New Jersey 07102, United States; orcid.org/0000-0003-0007-423X

Joshua Young — Department of Chemical & Materials Engineering, New Jersey Institute of Technology, Newark, New Jersey 07102, United States; orcid.org/0000-0001-

Jenny V. Lockard — Department of Chemistry, Rutgers, the State University of New Jersey, Newark, New Jersey 07102, United States; Occid.org/0000-0001-7758-169X

Eric Garfunkel – Department of Chemistry and Chemical Biology, Rutgers University, New Brunswick, New Jersey 08901, United States

Jianan Gao — Department of Civil and Environmental Engineering, New Jersey Institute of Technology, Newark, New Jersey 07102, United States; Oorcid.org/0000-0003-1255-1240

Complete contact information is available at: https://pubs.acs.org/10.1021/acscatal.4c00223

Author Contributions

[#]Q.L., O.K.K., and Q.M. contributed equally to this study. Qingdong Li and Oguz Kaan Kucukosman: Conceptualization of the research idea of P doping of WO3 as electrochemical catalyst for eNRR, fabrication, physical characterization, and evaluation of eNRR performance and HER activities of the catalysts. Writing-the original draft of the manuscript. Qingqua Ma: Theoretical calculation and writing the original draft of this section. Junjie Ouyang: Design and preparation of electrochemical cells via 3D printing. Zhiyuan Zhang: characterization of the catalysts. Pavel Kucheryavy: NMR characterization and writing the original draft of NMR related sections. Hengfei and Eric Garfunkel: XPS characterization, data collections, and fitting and writing the related sections. Conor L Long and Jenny V Lockard: XANES data collection, analysis, and writing the related sections. Joshua Young: supervision of the theoretical studies. Jianan Gao: drawing the TOC figure. Wen Zhang: project administration for the theoretical studies, reviewing, and editing of the manuscript. Huixin He: Supervision, project administration, funding acquisition for this project, writing, reviewing, and editing of the manuscript.

Notes

The authors declare no competing financial interest.

ACKNOWLEDGMENTS

We acknowledge Prof. Rich Mendelson and Dr. Carol Flach for the initial help for the Raman spectroscopic studies of the catalysts. This study was supported by the US National Science Foundation (Award #: 1742807 and 2215387), the US National Science Foundation (NSF)-MRSEC program (DMR-1420541), and Rutgers Research Council. DFT calculations were performed on the Lochness cluster at the New Jersey Institute of Technology, and the CARBON cluster at the Center for Nanoscale Materials under allocations CNM72868, CNM77374, and CNM79443. Computational work performed at the Center for Nanoscale Materials, a U.S. Department of Energy Office of Science User Facility, was supported by the U.S. DOE, Office of Basic Energy Sciences, under Contract no. DE-AC02-06CH11357. This research used Beamline 8BM (TES) of the National Synchrotron Light Source II, a U.S. Department of Energy (DOE) Office of Science User Facility operated for the DOE Office of Science by Brookhaven National Laboratory under Contract no. DE-SC0012704. Beamline operations were supported in part by the Synchrotron Catalysis Consortium (U.S. DOE, Office of Basic Energy Sciences, grant no. DE-SC0012335). We thank SCC scientist, Nebojsa Marinkovic for measurement of P Kedge XANES spectra.

REFERENCES

- (1) Ammonia Market Size & Share Analysis—Growth Trends & Forecasts (2024–2029); Mordor Intelligence, 2021, access date, 01 2023. https://www.mordorintelligence.com/industry-reports/ammonia-market.
- (2) Bharthwaj, A.; Hazarika, S.; Tufail, A.; Manoj, N.; Siva, A.; Ron, G. Coal gasification technology for ammonia plants. *Nitrogen & Syngas Conference*: Athens, Greece, 2012.
- (3) Foster, S. L.; Bakovic, S. I. P.; Duda, R. D.; Maheshwari, S.; Milton, R. D.; Minteer, S. D.; Janik, M. J.; Renner, J. N.; Greenlee, L. F. Catalysts for nitrogen reduction to ammonia. *Nat. Catal.* **2018**, *1* (7), 490–500.

- (4) Glibert, P. M.; Maranger, R.; Sobota, D. J.; Bouwman, L. The Haber Bosch-harmful algal bloom (HB-HAB) link. *Environ. Res. Lett.* **2014**, 9 (10), 105001.
- (5) Chen, J. G.; Crooks, R. M.; Seefeldt, L. C.; Bren, K. L.; Bullock, R. M.; Darensbourg, M. Y.; Holland, P. L.; Hoffman, B.; Janik, M. J.; Jones, A. K.; Kanatzidis, M. G.; King, P.; Lancaster, K. M.; Lymar, S. V.; Pfromm, P.; Schneider, W. F.; Schrock, R. R. Beyond Fossil Fuel-Driven Nitrogen Transformations. *Science* **2018**, *360* (6391), No. eaar6611.
- (6) Erisman, J. W.; Sutton, M. A.; Galloway, J.; Klimont, Z.; Winiwarter, W. How a century of ammonia synthesis changed the world. *Nat. Geosci.* **2008**, *1* (10), 636–639.
- (7) Hao, Y.-C.; Guo, Y.; Chen, L.-W.; Shu, M.; Wang, X.-Y.; Bu, T.-A.; Gao, W.-Y.; Zhang, N.; Su, X.; Feng, X.; Zhou, J.-W.; Wang, B.; Hu, C.-W.; Yin, A.-X.; Si, R.; Zhang, Y.-W.; Yan, C.-H. Promoting Nitrogen Electroreduction to Ammonia with Bismuth Nanocrystals and Potassium Cations in Water. *Nat. Catal.* 2019, 2 (5), 448–456.
- (8) Suryanto, B. H. R.; Du, H.-L.; Wang, D.; Chen, J.; Simonov, A. N.; MacFarlane, D. R. Challenges and prospects in the catalysis of electroreduction of nitrogen to ammonia. *Nat. Catal.* **2019**, *2* (4), 290–296.
- (9) Hatzell, M. C. A Decade of Electrochemical Ammonia Synthesis. *ACS Energy Lett.* **2022**, *7* (11), 4132–4133.
- (10) Zhang, S.; Zhang, X.; Rui, Y.; Wang, R.; Li, X. Recent advances in non-precious metal electrocatalysts for pH-universal hydrogen evolution reaction. *Green Energy Environ.* **2021**, *6* (4), 458–478.
- (11) Yang, C.; Zhu, Y.; Liu, J.; Qin, Y.; Wang, H.; Liu, H.; Chen, Y.; Zhang, Z.; Hu, W. Defect engineering for electrochemical nitrogen reduction reaction to ammonia. *Nano Energy* **2020**, *77*, 105126.
- (12) Wang, F.; Liu, Y.-p.; Zhang, H.; Chu, K. CuO/Graphene Nanocomposite for Nitrogen Reduction Reaction. *ChemCatChem* **2019**, *11* (5), 1441–1447.
- (13) Han, J.; Liu, Z.; Ma, Y.; Cui, G.; Xie, F.; Wang, F.; Wu, Y.; Gao, S.; Xu, Y.; Sun, X. Ambient N2 fixation to NH3 at ambient conditions: Using Nb2O5 nanofiber as a high-performance electrocatalyst. *Nano Energy* **2018**, *52*, 264–270.
- (14) Xian, H.; Guo, H.; Chen, Z.; Yu, G.; Alshehri, A. A.; Alzahrani, K. A.; Hao, F.; Song, R.; Li, T. Bioinspired Electrocatalyst for Electrochemical Reduction of N2 to NH3 in Ambient Conditions. ACS Appl. Mater. Interfaces 2020, 12 (2), 2445–2451.
- (15) Chu, K.; Liu, Y.-p.; Cheng, Y.-h.; Li, Q.-q. Synergistic borondopants and boron-induced oxygen vacancies in MnO2 nanosheets to promote electrocatalytic nitrogen reduction. *J. Mater. Chem. A* **2020**, 8 (10), 5200–5208.
- (16) Wang, X.; Li, S.; Yuan, Z.; Sun, Y.; Tang, Z.; Gao, X.; Zhang, H.; Li, J.; Wang, S.; Yang, D.; Xie, J.; Yang, Z.; Yan, Y. Optimizing Electrocatalytic Nitrogen Reduction via Interfacial Electric Field Modulation: Elevating D-Band Center in WS2-WO3 for Enhanced Intermediate Adsorption. *Angew. Chem., Int. Ed.* **2023**, 62 (29), No. e202303794.
- (17) Hoskuldsson, A. B.; Abghoui, Y.; Gunnarsdottir, A. B.; Skulason, E. Computational Screening of Rutile Oxides for Electrochemical Ammonia Formation. *ACS Sustainable Chem. Eng.* **2017**, 5 (11), 10327–10333.
- (18) Miu, E. V.; Mpourmpakis, G.; McKone, J. R. Predicting the Energetics of Hydrogen Intercalation in Metal Oxides Using Acid-Base Properties. ACS Appl. Mater. Interfaces 2020, 12 (40), 44658–44670.
- (19) Zheng, H. D.; Ou, J. Z.; Strano, M. S.; Kaner, R. B.; Mitchell, A.; Kalantar-Zadeh, K. Nanostructured Tungsten Oxide Properties, Synthesis, and Applications. *Adv. Funct. Mater.* **2011**, *21* (12), 2175–2196.
- (20) Wang, R.; Mitchell, J. B.; Gao, Q.; Tsai, W.-Y.; Boyd, S.; Pharr, M.; Balke, N.; Augustyn, V. Operando Atomic Force Microscopy Reveals Mechanics of Structural Water Driven Battery-to-Pseudocapacitor Transition. *ACS Nano* **2018**, *12* (6), 6032–6039.
- (21) Dong, D.; Benhaddouch, T. E.; Metler, C. L.; Marcial, J.; Zhao, Y.; Venkadesh, V.; Thundat, T.; Bhansali, S. Pseudocapacitive Charge

- Storage in Electrochromic Transition-Metal Oxide Thin Films. J. Electrochem. Soc. 2022, 169 (8), 080511.
- (22) Hjelm, A.; Granqvist, C. G.; Wills, J. M. Electronic structure and optical properties of WO3, LiWO3, NaWO3, and HWO3. *Phys. Rev. B* **1996**, *54* (4), 2436–2445.
- (23) Miu, E. V.; McKone, J. R.; Mpourmpakis, G. The Sensitivity of Metal Oxide Electrocatalysis to Bulk Hydrogen Intercalation: Hydrogen Evolution on Tungsten Oxide. *J. Am. Chem. Soc.* **2022**, 144 (14), 6420–6433.
- (24) Spencer, M. A.; Fortunato, J.; Augustyn, V. Electrochemical proton insertion modulates the hydrogen evolution reaction on tungsten oxides. *J. Chem. Phys.* **2022**, *156* (6), 064704.
- (25) Cui, X. Y.; Tang, C.; Zhang, Q. A Review of Electrocatalytic Reduction of Dinitrogen to Ammonia under Ambient Conditions. *Adv. Energy Mater.* **2018**, *8* (22), 1800369.
- (26) Zhang, L.; Ji, X. Q.; Ren, X.; Ma, Y. J.; Shi, X. F.; Tian, Z. Q.; Asiri, A. M.; Chen, L.; Tang, B.; Sun, X. P. Electrochemical Ammonia Synthesis via Nitrogen Reduction Reaction on a MoS2 Catalyst: Theoretical and Experimental Studies. *Adv. Mater.* **2018**, *30* (28), 1800191.
- (27) Nørskov, J. K.; Abild-Pedersen, F.; Studt, F.; Bligaard, T. Density functional theory in surface chemistry and catalysis. *Proc. Natl. Acad. Sci. U.S.A.* **2011**, *108* (3), 937–943.
- (28) Nilsson, A.; Pettersson, L. G. M.; Hammer, B.; Bligaard, T.; Christensen, C. H.; Nørskov, J. K. The electronic structure effect in heterogeneous catalysis. *Catal. Lett.* **2005**, *100* (3–4), 111–114.
- (29) Hu, L.; Xing, Z.; Feng, X. Understanding the Electrocatalytic Interface for Ambient Ammonia Synthesis. *ACS Energy Lett.* **2020**, 5 (2), 430–436.
- (30) Bon-Ryul, K.; Kim, K. H.; Ahn, H. J. Novel tunneled phosphorus-doped WO3 films achieved using ignited red phosphorus for stable and fast switching electrochromic performances. *Nanoscale* **2019**, *11* (7), 3318–3325.
- (31) Xu, J.; Liao, Z. H.; Zhang, J. B.; Gao, B.; Chu, P. K.; Huo, K. F. Heterogeneous phosphorus-doped WO3-x/nitrogen-doped carbon nanowires with high rate and long life for advanced lithium-ion capacitors. *J. Mater. Chem. A* **2018**, 6 (16), 6916–6921.
- (32) Chang, B.; Ai, Z. Z.; Shi, D.; Zhong, Y. Y.; Zhang, K.; Shao, Y. L.; Zhang, L.; Shen, J. X.; Wu, Y. Z.; Hao, X. P. p-n tungsten oxide homojunctions for Vis-NIR light-enhanced electrocatalytic hydrogen evolution. *J. Mater. Chem. A* **2019**, *7* (33), 19573–19580.
- (33) Sun, J.; Li, B.; Wang, Q.; Zhang, P.; Zhang, Y.; Gao, L.; Li, X. Preparation of phosphorus-doped tungsten trioxide nanomaterials and their photocatalytic performances. *Environ. Technol.* **2021**, 42 (26), 4104–4114.
- (34) Nayak, A. K.; Lee, S.; Choi, Y. I.; Yoon, H. J.; Sohn, Y.; Pradhan, D. Crystal Phase and Size-Controlled Synthesis of Tungsten Trioxide Hydrate Nanoplates at Room Temperature: Enhanced Cr(VI) Photoreduction and Methylene Blue Adsorption Properties. ACS Sustainable Chem. Eng. 2017, 5 (3), 2741–2750.
- (35) Choi, C.; Gu, G. H.; Noh, J.; Park, H. S.; Jung, Y. Understanding potential-dependent competition between electrocatalytic dinitrogen and proton reduction reactions. *Nat. Commun.* **2021**, *12* (1), 4353.
- (36) Zhu, Y.; Li, J.; Dong, C.-L.; Ren, J.; Huang, Y.-C.; Zhao, D.; Cai, R.; Wei, D.; Yang, X.; Lv, C.; Theis, W.; Bu, Y.; Han, W.; Shen, S.; Yang, D. Red Phosphorus Decorated and Doped Tio2 Nanofibers for Efficient Photocatalytic Hydrogen Evolution from Pure Water. Appl. Catal., B 2019, 255, 117764.
- (37) Chen, J.; Huang, S.; Long, Y.; Wu, J.; Li, H.; Li, Z.; Zeng, Y.-J.; Ruan, S. Fabrication of ZnO/Red Phosphorus Heterostructure for Effective Photocatalytic H₂ Evolution from Water Splitting. *Nanomaterials* (Basel, Switzerland) **2018**, 8 (10), 835.
- (38) Yan, J.; Wang, T.; Wu, G.; Dai, W.; Guan, N.; Li, L.; Gong, J. Tungsten Oxide Single Crystal Nanosheets for Enhanced Multichannel Solar Light Harvesting. *Adv. Mater.* **2015**, *27* (9), 1580–1586.
- (39) Ke, J.; Zhou, H.; Liu, J.; Duan, X.; Zhang, H.; Liu, S.; Wang, S. Crystal transformation of 2D tungstic acid H2WO4 to WO3 for

- enhanced photocatalytic water oxidation. *J. Colloid Interface Sci.* **2018**, *514*, *576*–*583*.
- (40) Zheng, R.; Lin, L.; Xie, J.; Zhu, Y.; Xie, Y. State of Doped Phosphorus and Its Influence on the Physicochemical and Photocatalytic Properties of P-doped Titania. *J. Phys. Chem. C* **2008**, *112* (39), 15502–15509.
- (41) Wang, F.; Di Valentin, C.; Pacchioni, G. Doping of WO3 for Photocatalytic Water Splitting: Hints from Density Functional Theory. *J. Phys. Chem. C* **2012**, *116* (16), 8901–8909.
- (42) Gu, H.; Zhang, F.; Hwang, S.; Laursen, A. B.; Liu, X.; Park, S. Y.; Yang, M.; Bramante, R. C.; Hijazi, H.; Kasaei, L.; Feldman, L. C.; Yeh, Y.; Batson, P. E.; Larson, B. W.; Li, M.; Li, Y.; Wyatt, K.; Young, J. L.; Teeluck, K.; Zhu, K.; Garfunkel, E.; Dismukes, G. C. Interfacial Connections between Organic Perovskite/n+ Silicon/Catalyst That Allow Integration of Solar Cell and Catalyst for Hydrogen Evolution from Water. *Adv. Funct. Mater.* 2023, 33 (25), 2301196.
- (43) Deb, S. K. Opportunities and challenges in science and technology of WO3 for electrochromic and related applications. *Sol. Energy Mater. Sol. Cells* **2008**, 92 (2), 245–258.
- (44) Cong, S.; Yuan, Y.; Chen, Z.; Hou, J.; Yang, M.; Su, Y.; Zhang, Y.; Li, L.; Li, Q.; Geng, F.; Zhao, Z. Noble Metal-Comparable SERS Enhancement from Semiconducting Metal Oxides by Making Oxygen Vacancies. *Nat. Commun.* **2015**, *6* (1), 7800.
- (45) Gahlawat, S.; Singh, J.; Yadav, A. K.; Ingole, P. P. Exploring Burstein-Moss type effects in nickel doped hematite dendrite nanostructures for enhanced photo-electrochemical water splitting. *Phys. Chem. Phys.* **2019**, *21* (36), 20463–20477.
- (46) Sun, Z.; Huo, R.; Choi, C.; Hong, S.; Wu, T.-S.; Qiu, J.; Yan, C.; Han, Z.; Liu, Y.; Soo, Y.-L.; Jung, Y. Oxygen Vacancy Enables Electrochemical N2 Fixation over WO3 with Tailored Structure. *Nano Energy* **2019**, *62*, 869–875.
- (47) Du, Y. Q.; Jiang, C.; Song, L.; Gao, B.; Gong, H.; Xia, W.; Sheng, L.; Wang, T.; He, J. P. Regulating surface state of WO3 nanosheets by gamma irradiation for suppressing hydrogen evolution reaction in electrochemical N-2 fixation. *Nano Res.* **2020**, *13* (10), 2784–2790.
- (48) Kong, W. H.; Zhang, R.; Zhang, X. X.; Ji, L.; Yu, G. S.; Wang, T.; Luo, Y. L.; Shi, X. F.; Xu, Y. H.; Sun, X. P. WO3 nanosheets rich in oxygen vacancies for enhanced electrocatalytic N-2 reduction to NH3. *Nanoscale* **2019**, *11* (41), 19274–19277.
- (49) Huang, J. E.; Li, F.; Ozden, A.; Sedighian Rasouli, A.; García de Arquer, F. P.; Liu, S.; Zhang, S.; Luo, M.; Wang, X.; Lum, Y.; Xu, Y.; Bertens, K.; Miao, R. K.; Dinh, C.-T.; Sinton, D.; Sargent, E. H. CO2 Electrolysis to Multicarbon Products in Strong Acid. *Science* **2021**, 372 (6546), 1074–1078.
- (50) Bard, A. J.; Faulkner, L. R. Electrochemical Methods: Fundamentals and Applications; John Wiley & Sons, Inc, 2001.
- (51) van der Heijden, O.; Park, S.; Eggebeen, J. J. J.; Koper, M. T. Non-Kinetic Effects Convolute Activity and Tafel Analysis for the Alkaline Oxygen Evolution Reaction on NiFeOOH Electrocatalysts. *Angew. Chem., Int. Ed.* **2023**, *62* (7), No. e202216477.
- (52) Qing, G.; Ghazfar, R.; Jackowski, S. T.; Habibzadeh, F.; Ashtiani, M. M.; Chen, C.-P.; Smith, M. R., III; Hamann, T. W. Recent advances and challenges of electrocatalytic N2 reduction to ammonia. *Chem. Rev.* **2020**, *120* (12), 5437–5516.
- (53) Chen, Z.; Liu, C.; Sun, L.; Wang, T. Progress of Experimental and Computational Catalyst Design for Electrochemical Nitrogen Fixation. *ACS Catal.* **2022**, *12*, 8936–8975.
- (54) Xue, Z.; Zhang, X.; Qin, J.; Liu, R. High-throughput identification of high activity and selectivity transition metal single-atom catalysts for nitrogen reduction. *Nano Energy* **2021**, *80*, 105527.
- (55) Guo, H.; Zhang, H.; Zhao, J.; Yuan, P.; Li, Y.; Zhang, Y.; Li, L.; Wang, S.; Song, R. Two-dimensional WO3-transition-metal dichalcogenide vertical heterostructures for nitrogen fixation: A photo (electro) catalysis theoretical strategy. *J. Phys. Chem. C* **2022**, *126* (6), 3043–3053.
- (56) Liu, Y.; Han, M.; Xiong, Q.; Zhang, S.; Zhao, C.; Gong, W.; Wang, G.; Zhang, H.; Zhao, H. Dramatically Enhanced Ambient Ammonia Electrosynthesis Performance by In-Operando Created Li-S

Interactions on MoS2 Electrocatalyst. Adv. Energy Mater. 2019, 9 (14), 1803935.